AGU PUBLICATIONS

JGR

Journal of Geophysical Research: Space Physics

RESEARCH ARTICLE
10.1002/2015JA021934

Key Points:
- Radar-based climatology of equatorial vertical drifts and spread *F* for past two solar cycles
- New insights on the relationship between evening drifts and equatorial spread *F*
- Strong and long-lasting equatorial *F* region structuring during sudden stratospheric warming events

Correspondence to:
F. S. Rodrigues,
Fabiano@utdallas.edu

Citation:
Smith, J. M., F. S. Rodrigues, B. G. Fejer, and M. A. Milla (2016), Coherent and incoherent scatter radar study of the climatology and day-to-day variability of mean *F* region vertical drifts and equatorial spread *F*, *J. Geophys. Res. Space Physics*, *121*, 1466–1482, doi:10.1002/2015JA021934.

Received 18 SEP 2015
Accepted 22 DEC 2015
Accepted article online 28 DEC 2015
Published online 3 FEB 2016

Coherent and incoherent scatter radar study of the climatology and day-to-day variability of mean *F* region vertical drifts and equatorial spread *F*

J. M. Smith[1], F. S. Rodrigues[1], B. G. Fejer[2], and M. A. Milla[3]

[1]William B. Hanson Center for Space Sciences, University of Texas at Dallas, Richardson, Texas, USA, [2]Center for Atmospheric and Space Science, Utah State University, Logan, Utah, USA, [3]Jicamarca Radio Observatory, Lima, Peru

Abstract We conducted a comprehensive analysis of the vertical drifts and equatorial spread *F* (ESF) measurements made by the Jicamarca incoherent scatter radar (ISR) between 1994 and 2013. The ISR measurements allowed us to construct not only updated climatological curves of quiet-time vertical plasma drifts but also time-versus-height maps of ESF occurrence over the past two solar cycles. These curves and maps allowed us to better relate the observed ESF occurrence patterns to features in the vertical drift curves than previously possible. We identified an excessively high occurrence of post-midnight *F* region irregularities during December solstice and low solar flux conditions. More importantly, we also found a high occurrence of ESF events during sudden stratospheric warming (SSW) events. We also proposed and evaluated metrics of evening enhancement of the vertical drifts and ESF occurrence, which allowed us to quantify the relationship between evening drifts and ESF development. Based on a day-to-day analysis of these metrics, we offer estimates of the minimum pre-reversal enhancement (PRE) peak (and mean PRE) values observed prior to ESF development for different solar flux and seasonal conditions. We also found that ESF irregularities can reach the altitudes at least as high as 800 km at the magnetic equator even during low solar flux conditions.

1. Introduction

Equatorial spread *F* (ESF) is the name given to signatures of ionospheric *F* region electron density irregularities observed using different types of measurements made at equatorial and low magnetic latitudes [*Booker and Wells*, 1938; *Hysell*, 2000; *Woodman*, 2009]. The scale size of these irregularities ranges from a few centimeters to hundreds of kilometers [*Basu et al.*, 1978; *Kelley et al.*, 1982]. Interchange plasma instabilities developing at the magnetic equator around sunset hours are invoked to explain the development of ESF irregularities [*Woodman and La Hoz*, 1976; *Sultan*, 1996]. The ionospheric generalized Rayleigh-Taylor (GRT) plasma instability finds ionospheric conditions at the magnetic equator around sunset hours leading to positive linear growth rates. The GRT explains most of the features observed during large-scale (greater than tens of kilometers) ESF events [*Woodman and La Hoz*, 1976; *Sultan*, 1996] and is often referred to as the source of ESF.

Several theoretical and experimental studies have investigated the genesis, development, and decay of ESF. These studies have indicated that the development of ESF is controlled by a number of factors including, in particular, the magnitude of the pre-reversal enhancement (PRE) of the equatorial zonal electric field [*Fejer et al.*, 1999], the occurrence/absence of plasma waves in the bottomside equatorial *F* region [*Kelley et al.*, 1981; *Huang and Kelley*, 1996; *Abdu et al.*, 2009], and the amplitude of meridional thermospheric winds [*Maruyama and Matuura*, 1984; *Krall et al.*, 2009]. An interchange plasma instability such as the GRT, operating in the equatorial *F* region, requires an initial perturbation to be triggered. Some studies suggest that this initial perturbation would be always present and would not affect the day-to-day or longer-term variability in the occurrence of ESF [*Su et al.*, 2008; *Retterer and Gentile*, 2009]. Other studies, however, propose that the amplitude and occurrence of the seed waves is variable and might be important in controlling the variability in ESF [*Kelley et al.*, 1981; *Abdu et al.*, 2009]. Most of these studies suggest that atmospheric gravity waves play an important role in generating the seed waves. For example, *Tsunoda* [2010] determined that gravity waves are linked to the occurrence/non-occurrence of ESF during solstice months in all longitude sectors. However, other sources of perturbations that could invoke ESF have also been suggested. Some studies have indicated that perturbations in the bottomside *F* region can be produced by the vertical shear in the zonal plasma

flow associated with the evening plasma vortex [*Hysell and Kudeki*, 2004; *Kudeki et al.*, 2007]. It has also been proposed that meridional thermospheric winds can affect the development of ESF [*Maruyama and Matuura*, 1984]. This hypothesis is, however, based on theoretical expectations of the long-term (interannual) variability of the winds and climatological studies of ESF occurrence at different longitude sectors. Experimental investigations of the effects of winds on the day-to-day variability of ESF, however, did not find conclusive evidence that meridional winds can suppress or stabilize the ESF growth [*Mendillo et al.*, 2001].

Finally, several studies have indicated that the magnitude of the PRE is the main parameter controlling the development of ESF [*Fejer et al.*, 1999; *Basu et al.*, 1996; *Abdu*, 2001; *Anderson et al.*, 2004]. In many such studies, it has been suggested that the PRE of significant magnitude (usually 20 m/s or more) is a necessary condition for ESF development [e.g., *Basu et al.*, 1996; *Abdu*, 2001]. Recently, *Huang and Hairston* [2015] examined this problem using satellite measurements of plasma drifts and ion density made on consecutive orbits. They showed that the occurrence of ESF structures increases with the magnitude of the PRE, with 83% of deep depletions occurring when the PRE is greater than 30 m/s.

Here we investigate the role of the PRE on ESF development using collocated, ground-based radar measurements of vertical plasma drifts and ESF irregularities. We take advantage of unique radar measurements made over nearly two solar cycles at the Jicamarca Radio Observatory (JRO). We used the drift mode observations and analyses available after 1994. These measurements were processed using the incoherent scatter radar (ISR) technique developed by *Kudeki et al.* [1999], which allowed for accurate measurements of plasma drifts not only in the main *F* region but also in the bottomside and topside *F* region. The mode also allowed for measurements of drifts during nighttime that are more accurate than previously possible. Finally, the pointing position of the mode (near perpendicular to the geomagnetic field) allows simultaneous detection of coherent scatter echoes and, therefore, the detection of the occurrence and morphology of ESF events. The Jicamarca measurements allowed us to estimate the climatological variations of mean *F* region drifts and the occurrence (as a function of local time and height) of ESF irregularities. With these new measurements, we have provided newly updated seasonal- and solar-flux- averaged drift curves and ESF estimates over the last two solar cycles. The measurements also allowed us to investigate, on a day-to-day basis, the relationship between the PRE peak and the development of ESF.

Our study is presented as follows: In section 2, we describe the measurements and our approach of analysis. We present the results of our analyses and discuss these results in section 3. Section 4 summarizes our findings and main conclusions.

2. Measurements and Analyses

2.1. Measurements

We used incoherent scatter radar (ISR) measurements to accurately determine the intensity of the pre-reversal enhancement (PRE) of the evening zonal equatorial electric field (i.e., vertical plasma drift). The occurrence and morphology (local time versus height) of ionospheric irregularities were determined from ISR measurements contaminated by coherent scatter echoes, that is, echoes from field-aligned irregularities.

The measurements were made by the ISR of the Jicamarca Radio Observatory (11.95°S, 76.87°W) near the magnetic equator. Despite the importance of *F* region ionospheric drifts, Jicamarca is the only magnetic equatorial site capable of making accurate and unambiguous measurements of both the vertical and zonal drifts as a function of time and height. The ISR technique uses scattering of radio waves by thermal electron density fluctuations to determine the background plasma velocity. The incoherent scatter spectrum is very narrow when the radar beam's pointing direction is close to perpendicular with the geomagnetic field [*Sulzer and Gonzalez*, 1999]. While this makes the derivation of plasma parameters (e.g., ion composition, temperatures) from ISR measurements more difficult, it allows for extremely accurate line-of-site drift measurements [*Kudeki et al.*, 1999]. Therefore, two separate modes are used when determining ISR parameters and drifts.

Until about 1994, measurements of the ionospheric drifts at Jicamarca were made using the pulse-to-pulse correlation method [*Woodman and Hagfors*, 1969]. The technique allowed measurements of drifts with an accuracy up to 2 m/s but only around *F* region peak heights where the signal-to-noise ratio (SNR) is greatest. The long-term measurements made by this method allowed great advances in our understanding of the *F* region equatorial drifts. For example, the *Scherliess and Fejer* [1999] climatological model of equatorial vertical drifts was developed using these measurements. *Kudeki et al.* [1999] introduced a new approach

for estimating ionospheric drifts. This new technique is based on Doppler spectra estimation and nonlinear squares fitting of the incoherent scatter spectrum to the measurements. While more computationally intensive, the new method allowed for more accurate measurements of the drifts when the SNR is low. This new technique greatly improved the drift measurements made during nighttime and in the bottomside *F* region. Furthermore, the new method provided drift measurements with uncertainties in the line-of-sight direction as low as 0.5–1.0 m/s.

The vertical (and zonal) component of ionospheric *F* region drifts are obtained, unambiguously, from line-of-sight measurements made by two independent radar beams. The setup is such that the two beams are pointed a few degrees toward the east and west. By combining the two line-of-sight measurements, the vertical and zonal components of the drifts are obtained. Due to the high cost associated with the operation of MegaWatt ISRs and the fact that the radar hardware is also used for other types of atmospheric measurements, only ~10–15 days per year of drift measurements are usually made.

ISR drift measurements made at Jicamarca between 1994 and 2013 under the *Kudeki et al.* [1999] mode were used for this study. The measurements cover different geophysical conditions over, approximately, two solar cycles. Careful inspection of the data files show that measurements for 381 different days are available. In general, files with information about the vertical drifts, as a function of time and height, were available for this study. The measurements generally start at *E* region heights and go up to 800–1000 km depending on solar flux conditions. Therefore, the radar can probe echoes associated with structures that, if field-aligned, can reach roughly 17–19° magnetic latitude. Typical range and time resolutions are about 15 km and 5 min, respectively. Note that the amount of measurements varies from day to day. While some days have full 24 h of measurements, other days have only a few hours of observations available.

Additional parameters, such as uncertainties in the drift estimates, were also provided with the measurements. The SNR of incoherent and coherent scatter echoes were also available. Of particular importance to this study, is the information associated with the coherent SNR. Coherent scatter echoes (tens of decibels above thermal levels) compromise ISR drift measurements, but serve as a reliable tracer of ESF occurrence. In our analyses, we use ISR measurements to determine the behavior of the *F* region drifts and coherent scatter radar (CSR) measurements to determine the behavior of ESF for a given evening.

2.2. Analysis

Our investigation of the relationship between the PRE and topside irregularities requires nearly continuous measurements between 1700 and 2400 LT. To meet our criteria, each observation day could only have had a data gap in the drift measurements, between 1700 and 2000 LT, that did not exceed 45 min (25% of the time window). Also, each observation day could only have had a gap in the incoherent/coherent scatter SNR measurements, between 1900 and 2400 LT, that did not exceed 1.25 h (25% of the time window). Finally, only measurements where the *Kp* at the time of the measurement and three previous values did not exceed 4 were used to assure that only observations made during geomagnetically quiet conditions were taken into consideration. Our selection criteria resulted from the best compromise between data quality and availability.

Figure 1 shows an example that illustrates the measurements and our analysis procedure. Each panel is a two-dimensional (local time versus height) representation of the following parameters: (a) SNR (actually SNR + 1 in decibels) of coherently scattered echoes, (b) vertical plasma drifts, (c) estimated location (local time versus range map) of the occurrence of field-aligned irregularities (red indicates echoes, blue indicates no echoes), and (d) estimated mean *F* region vertical drifts. The occurrence of irregularities (as shown in Figure 1c) was determined through the occurrence of coherent echoes in 15 min time and 30 km height intervals. The occurrence of coherent echoes was based on coherent scatter SNR values. We assume that ESF irregularities occurred when at least two or more coherent echoes with SNR + 1 greater than 10 dB were observed in each time/range interval. We found that requiring two or more echoes above a threshold of 10 dB in each time/range bin is not only a robust metric of irregularity occurrence but is also helpful in avoiding counting clutter echoes as ESF irregularities. Note that the red portion of the map (Figure 1c) is a very good indicator of times and heights of enhanced CSR echoes in Figure 1a. The mean *F* region drifts shown in Figure 1d were obtained by averaging ISR drift measurements between 200 and 400 km altitude at 15 min time intervals. Only drift measurements at times and heights when CSR echoes were not detected and with uncertainties less than 2 m/s were used in the averages. The error bars represent the variability (standard deviation) of the drift values used in each average. We point out that this is a new approach in defining the vertical drifts, where measurements are taken from bottomside altitudes only, i.e., at altitudes where the growth rate is maximized.

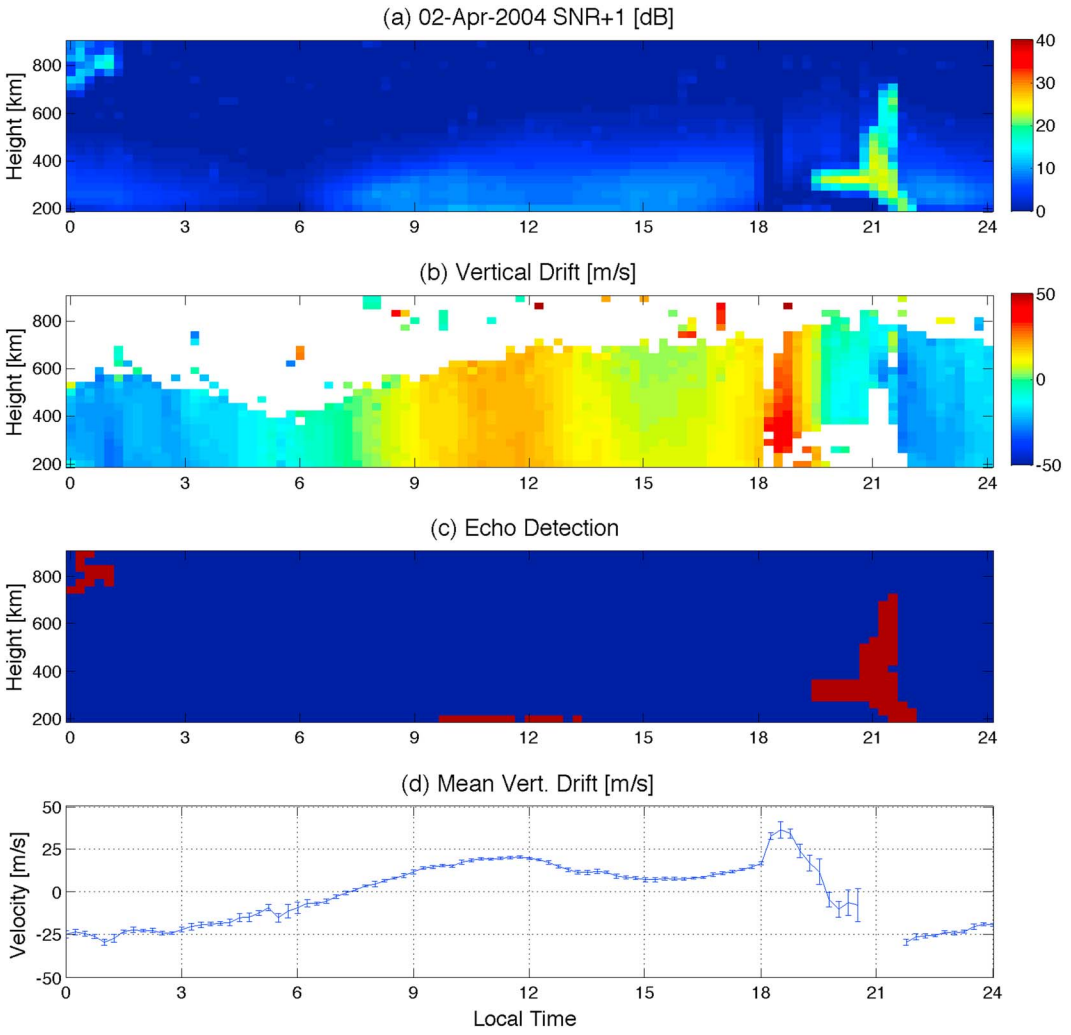

Figure 1. Example of measurements and analysis for 2 April 2004. (a) Signal-plus-noise power over noise [(S + N)/N] of coherently scattered echoes, (b) ISR vertical drifts, (c) time versus height map of coherent scatter echoes/irregularities (red/blue indicates the occurrence/non-occurrence of irregularities, respectively), and (d) mean *F* region vertical drifts.

Figure 1d shows a typical example of the enhancement of the vertical drifts around sunset hours that is commonly observed at the magnetic equator. The vertical drifts start to increase around 1630 LT and reach a maximum value of 37 m/s around 1840 LT. Figures 1a and 1c show that *F* region coherent echoes indicating irregularities start around 1900 LT at approximately 350 km altitude. The echoes were confined to a narrow (in altitude) layer. The layer began to develop upward at around 2100 LT and reached altitudes above 800 km around 2130 LT. No measurements are usually available beyond ~900 km altitude.

Woodman and La Hoz [1976] and *Hysell and Burcham* [1998] pointed out that three main types of ESF echoing structures are most commonly observed in coherent scatter radar range-time-intensity (RTI) maps such as that shown in Figure 1b. The first type of echoing region is characterized by a narrow (in altitude) layer that stays well within the bottomside *F* region and does not develop in altitude. Results from interferometric radar studies showed that these narrow layers tend to move in the westward direction or very slowly in the eastward direction [*Hysell and Burcham*, 2002]. These types of echoing regions are referred to as bottom-type layers and are not produced by the Rayleigh-Taylor instability. Instead, they are believed to be caused by wind-driven gradient drift instabilities operating on unstable horizontal density gradients in the bottomside *F* region. The irregularities within these layers are produced by advection rather than convection [*Hysell et al.*, 2004]. Additionally, again based on imaging results, it has been found that bottom-type irregularities can also coexist with other types of ESF irregularities [e.g., *Rodrigues et al.*, 2012a]. The second type of echoing region seen in CSR RTI maps is referred to as the bottomside layer, which is characterized by an echoing region that

is more structured than the bottom-type layer. It also develops more vertically in altitude than bottom-type irregularities, but still remains in the bottomside *F* region. These layers serve as tracers of plasma depletions that did not fully develop, and the reason for this suppression is still unclear. Like bottom-type layers, bottomside layers also may not be associated with the Rayleigh-Taylor instability. However, it has been suggested that these types of echoing regions are the manifestation of the so-called collisional shear instability [*Aveiro and Hysell*, 2010]. This instability stems from a strong vertical shear in the zonal plasma drift velocity around the bottomside region [*Tsunoda et al.*, 1981], where these irregularities develop. The low-altitude echoes seen in Figures 1a and 1c between 1930 and 2030 LT could have been caused by bottom-type or bottomside irregularities.

Finally, the last type of echoing region is known as topside layers or plumes. Plumes are radar echo signatures of low-latitude ionospheric plasma depletions also known as equatorial plasma bubbles [e.g., *Woodman and La Hoz*, 1976]. Topside layers show as diagonal (and sometimes vertical) echoing channels starting at bottomside *F* region heights and reaching the topside. Therefore, topside echoes are often used as a tracer of the occurrence of fully developed ESF events. The echoing channel seen in Figures 1a and 1c around 2000 LT is caused by topside irregularities.

3. Results and Discussion

3.1. ESF Climatology

Figure 2 shows our maps of the occurrence rates of ESF irregularities as a function of local time and height for different seasons and three different levels of solar activity. The rates were determined using only observations made during geomagnetically quiet conditions. That is, only measurements made when the *Kp* index was equal or below 4, and the previous 3 *Kp* values also did not exceed 4. To compute the occurrence rates, we used our procedure for detection of irregularities (see previous section). For a given local time versus height bin, the rate represents the ratio of observations (i.e., days) indicating the occurrence of irregularities over the total number of observations. The bin resolution is 30 km in height and 15 min in local time. The number within square brackets indicates the number of observations used to construct each occurrence rate map. Note that the number of observation hours vary dramatically from day to day. While some days have almost 24 h of measurements, other days have only a couple of hours of valid observations. The solid black lines are isocontours of the 0.4 (40%) occurrence rates, which are shown for reference. We have organized the occurrence rate maps based on the following seasons: December solstice (November–January months), June solstice (May–July months), and equinox (February–April, August–October months). We also categorized the occurrence maps based on varying levels of solar activity, which was determined using the $F_{10.7}$ solar flux index. The levels represent low ($F_{10.7} < 100$ SFU), moderate ($100 \leq F_{10.7} \leq 140$ SFU) and high solar flux activity ($F_{10.7} > 140$ SFU). We will denote low solar flux as "LSF," moderate solar flux as "MSF," and high solar flux as "HSF." The season and solar activity level are indicated at the top of each panel.

It can be seen in Figure 2 that coherent echoes (from irregularities) only occur during nighttime (pre-midnight and post-midnight) hours. The occurrence rate maps for pre-midnight ESF, as expected from previous studies of equatorial ionospheric stability [e.g., *Watanabe and Oya*, 1986; *Kil and Heelis*, 1998], show the occurrence of irregularities starting around ~1900 LT and lasting, usually, until local midnight or longer. The highest rates can be seen during December solstice and the lowest rates during June solstice. Moderate occurrence rates are observed during equinox. We point out that a reduced number of days were available for December solstice compared to equinox. The pre-midnight results also indicate that the height at which irregularities are first observed to occur increases with solar flux activity. This is most evident in December solstice and equinox. For instance, during December solstice, first irregularities are observed around 240 km and 320 km altitude under LSF and HSF conditions, respectively. These results agree with theoretical expectations. As ESF is known to start in the bottomside *F* region [*Kelley*, 1989] and because the altitude of the *F* layer increases with solar flux activity [e.g., *Zhang et al.*, 1999], it is expected that ESF onset would also occur at higher altitudes. Our results are also in good agreement with previous experimental inferences obtained with more numerous observations made by the coherent backscatter radar mode of the Jicamarca Radio Observatory [*Chapagain et al.*, 2009].

Hysell and Burcham [2002] also presented an analysis of the occurrence rates of ESF irregularities measured by the Jicamarca Unattended Long-term Investigations of the Ionosphere and Atmosphere (JULIA) coherent scatter radar system. The analysis was carried out for measurements made between 1996 and 2000. JULIA is a low-power radar system that operates much more frequently than the incoherent scatter radar. ISR drift

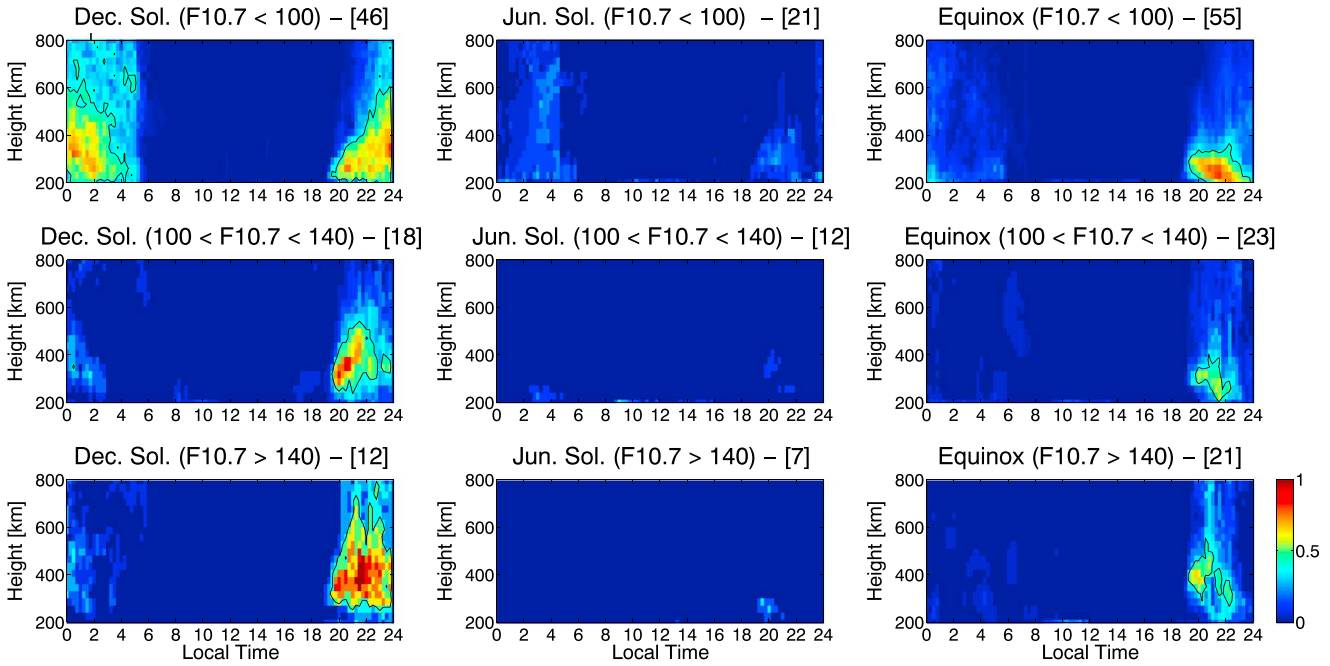

Figure 2. Occurrence rate of quiet-time *F* region echoes as a function of local time and height. Each panel represents a season and solar flux condition. The season and solar flux condition are indicated on top of each panel. The number within square brackets indicates the number of the different days when measurements were made. The black solid lines are isocontours of the 0.4 (40%) occurrence rates and are shown for reference.

measurements are only made 10–15 d/yr while JULIA ESF measurements are made over more than 200 d/yr. Our local time versus height morphology of ESF irregularities for December solstice is very similar to what they obtained from JULIA measurements. For instance, both studies found that, during LSF conditions, pre-midnight irregularities slowly reach topside heights, with significant occurrence rates only around local midnight. Irregularities reach the topside quicker as solar flux increases. Our results for equinox also resemble the *Hysell and Burcham* [2002] results but to a lesser degree. We found, in particular, a significant difference in occurrence rates between December and equinox, which is not clear in the JULIA results. Our higher occurrence rates in December led us to examine our observations in more detail. As a result, we found strong and long-lasting ESF events associated with sudden stratospheric warming (SSW) events. Since SSW events are associated with cause negative *F* region plasma drifts in the afternoon/evening sector [e.g., *Chau et al.*, 2009], one would have expected a decrease in the GRT linear growth rate and suppression of ESF development. We found, instead, that strong and long-lasting ESF events are commonly observed during SSW events. In the past several years, Jicamarca has performed campaigns of observations during SSW events, which were included in our analysis. Figure 3 shows, as an example, the measurements made during a period of SSW in January 2008 [e.g., *Chau et al.*, 2009]. This is a first look at the SNR estimates as made by the Jicamarca ISR during a SSW event. It shows that strong ESF occurred during the period of SSW and that the ESF events generally lasted well beyond local midnight. This implies, for the first time, that the semi-diurnal variations in the vertical drifts as seen during the daytime/evening sector [e.g., *Chau et al.*, 2009] may affect the PRE timing and development.

Another hypothesis for the high occurrence of ESF during December LSF is related to the abnormal thermospheric and ionospheric conditions of the extreme 2008/2009 solar minimum [e.g., *Heelis et al.*, 2009]. A combination of excessively low ionospheric densities and contracted thermosphere could lead to reduced ion-neutral collision frequencies and more favorable conditions for the GRT instability.

During June solstice, we observed a decrease of pre-midnight irregularities with solar flux. A few cases of topside echoes were observed during LSF conditions. During MSF and HSF conditions, however, only a few isolated cases of scattering structures, restricted to bottomside and main *F* region heights, have been detected. Our results agree with previous studies using different observational techniques, which found a higher occurrence of ESF in June solstice during LSF conditions [e.g., *Candido et al.*, 2011]. We found that, at times, favorable conditions for full development of ESF irregularities exist during June solstice but only during periods of LSF.

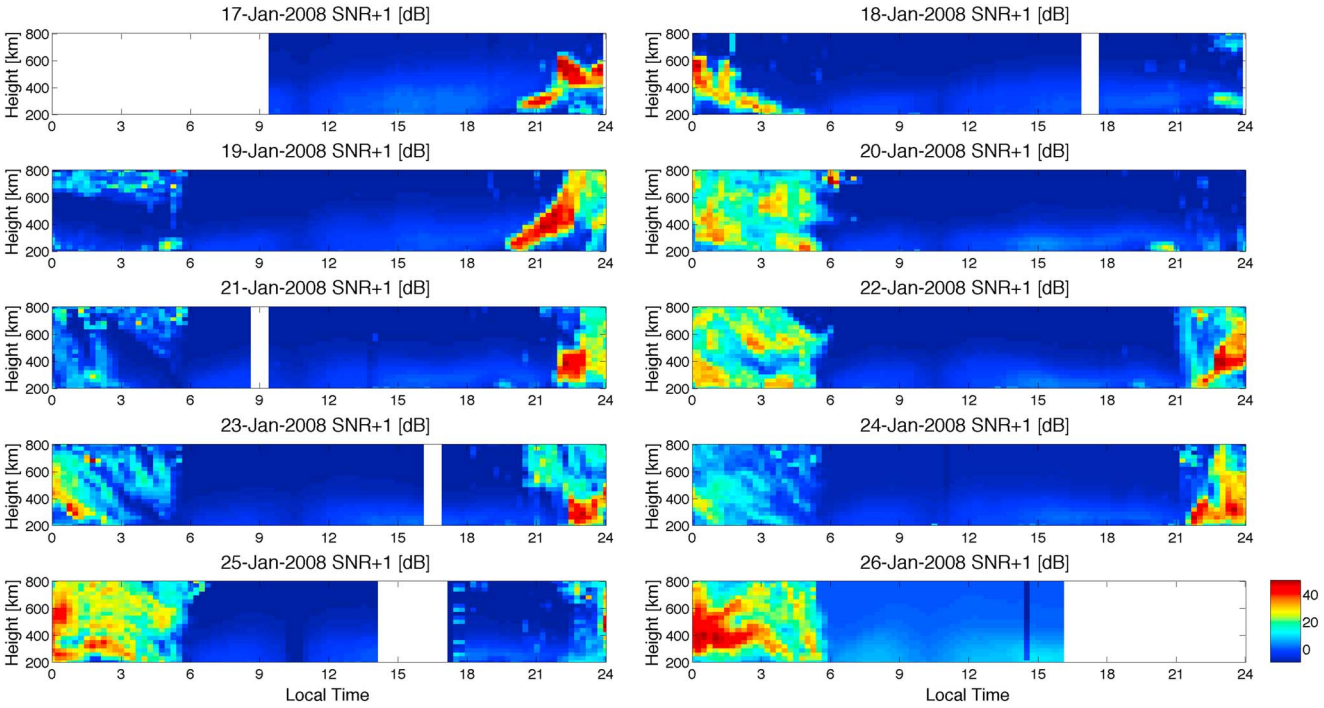

Figure 3. Coherent scatter radar echoes observed during the January 2008 sudden stratospheric warming (SSW) event.

Figure 2 also shows an increased occurrence rate of post-midnight irregularities during LSF conditions. During December solstice, in particular, occurrence rates are as high as 70% around main *F* region heights. Higher occurrence rates of post-midnight ESF during LSF conditions can also be observed during June solstice and equinox. The occurrence rates, however, did not exceed ~25%. Previous studies using different types of observational techniques also found a higher occurrence rate of post-midnight ESF during LSF years [*Huang et al.*, 2010]. *Hysell and Burcham* [2002] also found that the occurrence of irregularities would last longer during December solstice than equinox. They did not find occurrence rates of post-midnight irregularities as high as we found, particularly during LSF conditions. This could be caused by the fact that JULIA uses low-power transmitters and could not detect the weak post-midnight irregularities observed by the Jicamarca ISR. As mentioned earlier, this could also be due to the numerous ISR measurements made during SSW events.

Finally, close inspection of the maps in Figure 2 also show cases of irregularities occurring near sunrise. The large dynamic range of the color plots and the low occurrence rate of the sunrise echoes make their identification somewhat difficult. Nevertheless, one can see that the echoes tend to occur around main *F* region heights during equinox at around 0600–0700 LT and topside heights in December solstice, particularly, around 0600 LT. *Fejer et al.* [1999] used Jicamarca radar data and found that late night ESF are generally fully developed topside structures and possibly associated with a disturbed dynamo. However, *de La Beaujardiere et al.* [2009], using mostly geomagnetically quiet C/NOFS satellite data, discovered deep plasma depletions (i.e., strong ESF) near sunrise following enhancements in the vertical ion drift.

3.2. *F* Region Drift Climatology

In order to better understand the climatology of ESF, as observed by the Jicamarca radar, we also obtained daily curves of the mean *F* region vertical drifts from the incoherent scatter radar observations. Figure 4 shows the daily mean *F* region drift curves (between 200 and 400 km) that we have derived from the data sets available for this study (1994–2013). As we did for the occurrence rate maps, we also grouped geomagnetically quiet drift curves according to season and solar flux activity. There is a large daily variability in the behavior of the drift curves. Nevertheless, some main features can be easily distinguished and tend to follow expectations from previous theoretical and experimental studies of the low-latitude ionosphere electrodynamics [e.g., *Fesen et al.*, 2000; *Fejer et al.*, 2008; *Kil et al.*, 2009; *Rodrigues et al.*, 2012b]. The drifts are, in general, positive (upward) during the day and negative (downward) during nighttime. It is also possible to distinguish the enhancement of the vertical drifts around sunset hours prior to its reversal.

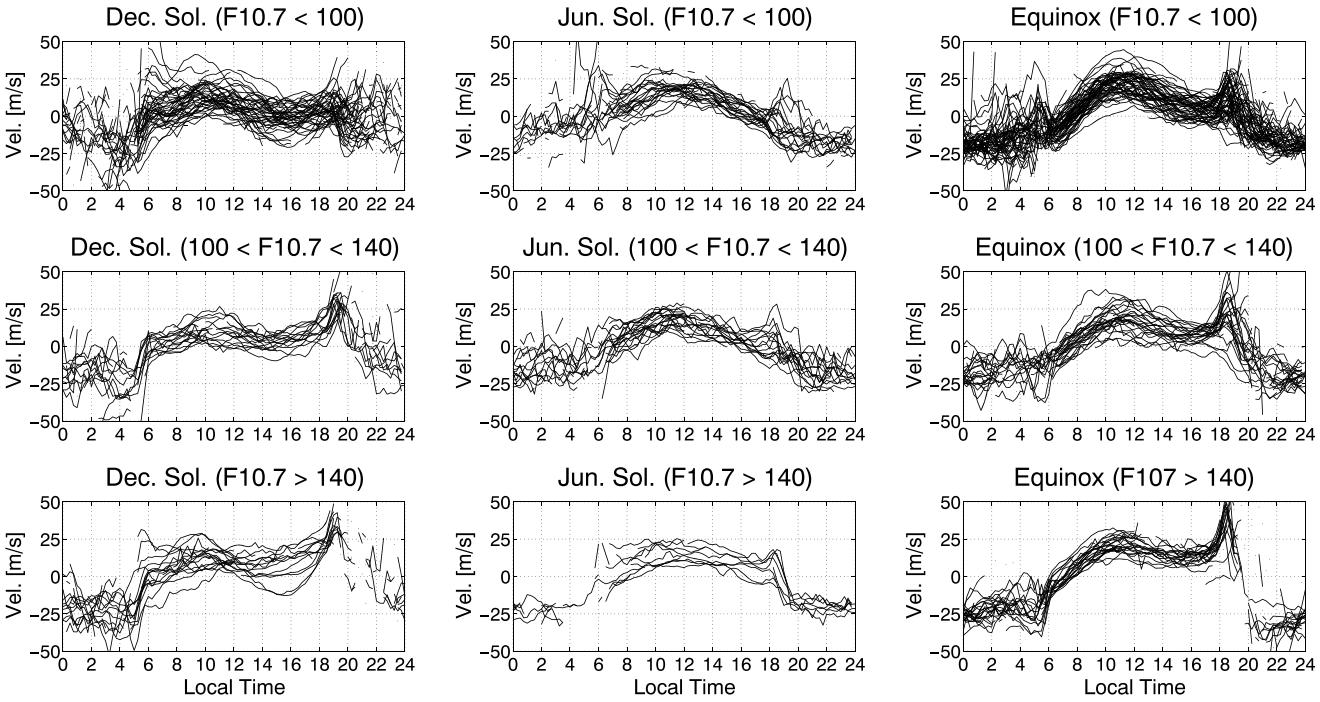

Figure 4. Daily curves of quiet-time mean *F* region (200–400 km) drifts as a function of local time. Each panel represents a season and solar flux condition. The season and solar flux condition are indicated on top of each panel.

We also computed season- and solar-flux-averaged vertical drift curves in order to better interpret the behavior of ESF climatology. Figure 5 shows these average curves, again, for three solar flux levels and seasons. The error bars indicate the variability (standard deviation) of the values used to compute the averages. The mean curves represent well our perception of the daily behavior of the curves shown in Figure 4. The mean curves show that the drifts are, mostly, upward during the day and downward during the night. The mean curves also show that the average peak of the PRE of the drifts occurs between 1700 and 2000 LT.

Figures 4 and 5 show that the PRE peak is well developed during December solstice and equinox. During June solstice, however, the PRE is weak or even absent. Relating the results shown in Figures 4 and 5 to the ESF occurrence rates maps in Figure 2, it follows that higher occurrences of pre-midnight ESF are correlated with enhancements of the PRE peak. Figure 2 shows higher occurrence rates for December and equinox, as opposed to June. This is expected as the PRE peak increases the linear growth rate of the Generalized Rayleigh-Taylor instability [*Sultan*, 1996; *Basu*, 2002] via large $\mathbf{E} \times \mathbf{B}$ vertical drifts. The PRE also moves the *F* layer to higher altitudes, where the ion-neutral collision frequency is reduced. This reduction in the collision frequency also leads to an increase in the GRT instability growth rate [*Jayachandran et al.*, 1993]. The mean vertical drift curves (Figure 5) also suggest that, on average, the post-reversal of the evening drifts are more sudden in equinox than in December. Additionally, the mean curves show that the downward drifts between ~2000 LT and midnight in equinox have larger magnitudes than the drifts in December. These features can also be observed in the mean drift curves presented by *Scherliess and Fejer* [1999], which were obtained from a completely independent set of measurements. The short duration of the PRE followed by large post-reversal downward drifts observed during equinox provide more stabilizing conditions than those of December. This stabilization explains the higher and longer-lasting occurrence of ESF in December compared to equinox.

We also observe solar flux effects on the PRE peak and ESF behavior. The magnitude of the PRE is often explained in terms of the magnitude of the component of the neutral wind in the magnetic zonal direction and longitudinal gradients in ionospheric conductivity [e.g., *Heelis et al.*, 1974]. Both parameters increase with solar flux, which leads, as a consequence, to larger PRE values during periods of HSF activity. The increase in PRE with solar flux is clearly observed during December solstice and equinox and leads to a greater number of ESF occurrences at higher altitudes. The PRE also becomes more noticeable with increasing solar flux during June solstice but still fairly weak. The magnitude of the post-PRE downward drifts, however, increases and the

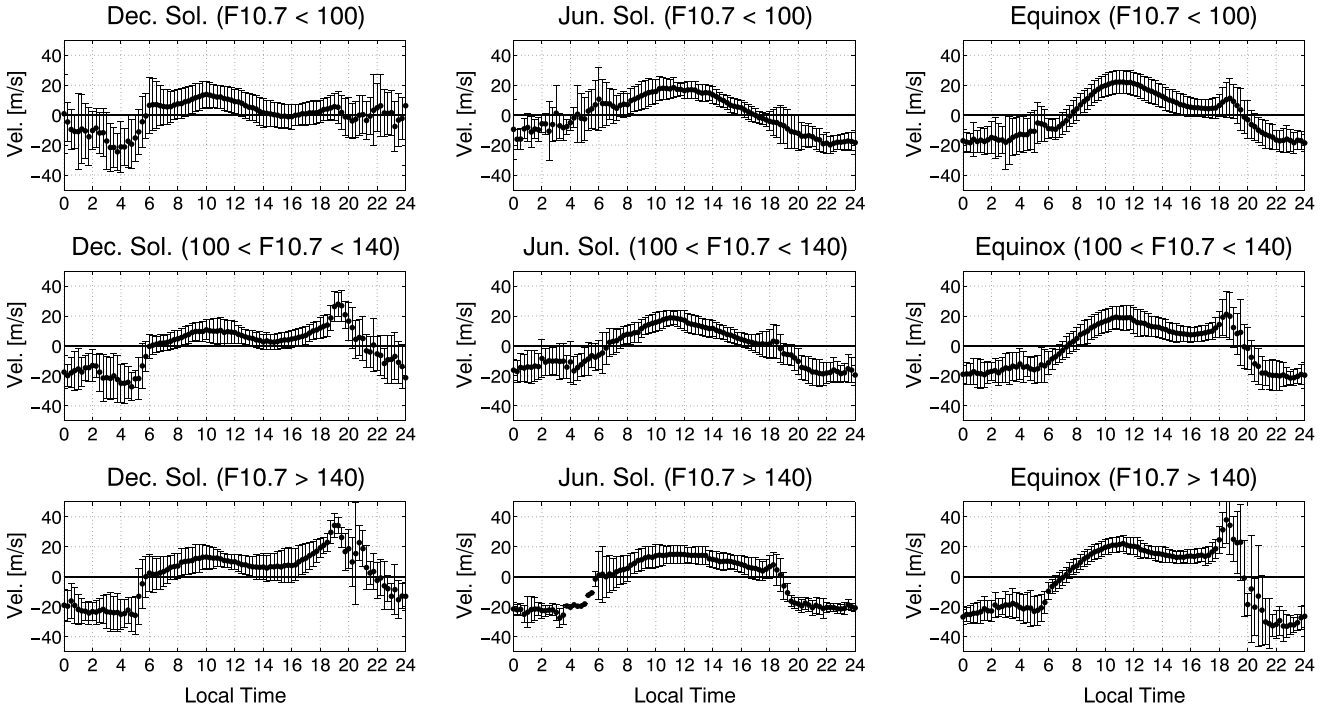

Figure 5. Climatological quiet-time curves of mean *F* region (200–400 km) drifts for 1994–2013 data sets. Each panel represents a season and solar flux condition. The season and solar flux condition are indicated on top of each panel.

transition from upward to downward drifts become more pronounced. This might explain the decrease of ESF occurrence with solar flux in June solstice.

We show the variability of the PRE peak as a function of solar flux for each season in Figure 6. We have estimated the PRE peak from the daily curves of the mean *F* region drifts in Figure 4. One can see that the likelihood of observing larger magnitudes of the PRE peak increases with solar flux, particularly, in December and equinox. The solar flux effect is not as clear in June but still present.

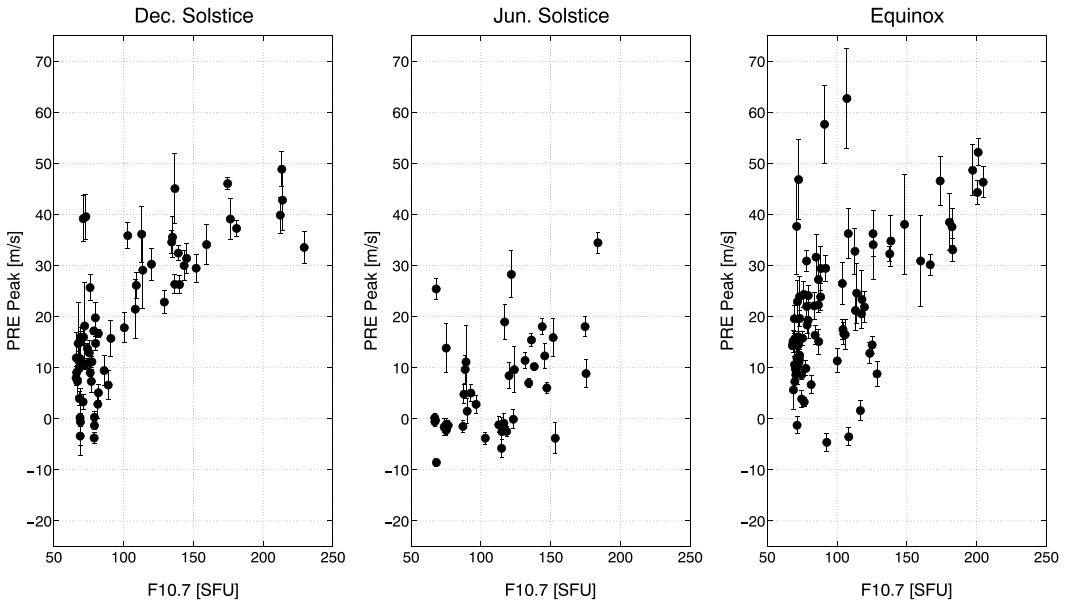

Figure 6. Quiet-time PRE peak values as a function of solar flux ($F_{10.7}$ index) for each season considered in this study.

Even during low solar flux conditions, ESF can be observed with a significant occurrence rate. The atmosphere is more contracted during low solar activity, requiring less upward drifts to lift the ionosphere to unstable conditions (low ion-neutral collision frequency). The observed high occurrence, long duration, and altitude reach of ESF during December solstice LSF, however, is unusual if compared to previous studies. Previous studies show a lower occurrence of post-midnight echoes [*Hysell and Burcham*, 2002]. As mentioned earlier, we associate our detection of a higher occurrence of ESF to the high sensitivity of the Jicamarca ISR. *Hysell and Burcham* [2002] used measurements of a low-power mode (JULIA) coherent scatter mode of the Jicamarca radar. Also, the data set used in the present study included a large number of measurements made around SSW events, which were made in recent years as part of SSW observation campaigns. The measurements analyzed by *Hysell and Burcham* [2002] were limited to a period between 1996 and 2000. Finally, the observations used in this study used included a period of abnormally low solar flux conditions (2008–2009), which led to a more contracted ionosphere than previously observed.

The mean vertical drifts can also explain the post-midnight behavior of ESF. For instance, Figure 2 shows a decrease in the occurrence rates of post-midnight ESF as solar flux increases for December solstice and equinox. The observed post-midnight ESF occurrence is associated with irregularities generated in the pre-midnight sector. We associate the reduction in post-midnight ESF occurrence with the stronger stabilizing effect of larger downward drifts and increased ion-neutral collision frequencies during periods of higher solar activity. The downward motion might also cause more damping of electron density irregularities via enhanced recombination rates.

3.3. PRE and ESF: Day-to-Day Variability

The collocated incoherent and coherent scatter measurements allow us to investigate, in more detail, the role of the evening drifts in the occurrence of pre-midnight ESF. In order to proceed with a day-to-day analysis, we defined metrics for both ESF development strength and evening upward drifts. These metrics are intended to better assess the ESF response to the behavior of the evening vertical drifts.

First, we describe the two metrics of ESF intensity used in this study. These are newly proposed metrics, which have been automated for practicality purposes. The first metric is based on height and local time occurrence of ESF. The metric is defined as the percentage of bins between 1900 and 2400 LT and between 200 and 800 km altitude, where irregularities were detected. For instance, if ESF did not occur and echoes were not detected, the metric value would be 0. On the other hand, a hypothetical ESF event, causing irregularities at all times between 1900 and 2400 LT and reaching all altitudes in this time interval would produce a metric value of 1. This is a very practical metric and represents the occurrence of ESF, not only in time but also in height, observed at a fixed location, that is, over Jicamarca. We refer to this metric as "ESF occurrence index." The second metric of ESF is one based on the maximum height of the observed echoes. Therefore, the metric values would range between 200 and 800 km or 0 (no ESF at all). We remind the reader that 800 km is the maximum altitud probed in typical ISR measurements. This metric represents ESF vertical development. Bottom-type and bottomside events would produce metric values ranging between 200 and 500 km, while topside events would produce metric values ranging, typically, between 500 and 800 km. We refer to this metric as "ESF maximum height" or simply "ESF max height."

Next, we explain two distinct metrics that represent the magnitude of the PRE and were used in this study. The first PRE metric aims to define the magnitude of the PRE peak. For each daily mean *F* region drift curve (Figure 1d), we found the magnitude of PRE, which is the maximum value of the vertical drift between 1700 and 2000 LT. We refer to this metric as the "PRE peak." The second metric attempts to take into consideration the history of the evening drifts for a correlation study with ESF. *Stolle et al.* [2008], for example, pointed out the importance of the history of the drifts for ESF development. Upward drifts starting in the late afternoon could contribute to creating favorable conditions for GRT instability growth. The upward drifts, even with small magnitudes, would contribute by moving the *F* layer to regions of reduced ion-neutral collisions [*Huang et al.*, 2012]. Additionally, as mentioned earlier, large negative drifts immediately following the PRE would suppress the GRT instability growth. With these considerations in mind, we defined our second metric as the "mean PRE," computed as the average of the vertical drifts between 1700 and 2000 LT.

Figures 7–10 show the results of our analyses of the PRE versus ESF development for different seasons and solar flux conditions. The results are shown only for observation days when at least 75% of the drift measurements between 1700 and 2000 LT are available and considered of good quality. We discarded,

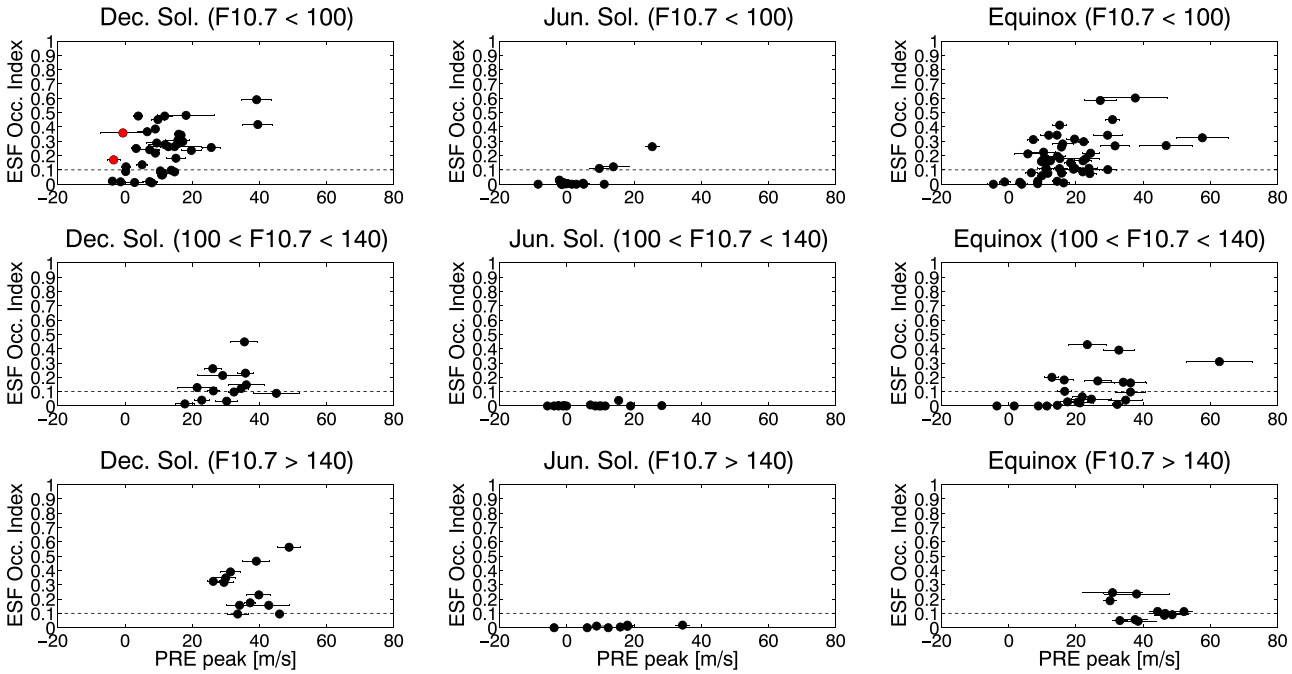

Figure 7. PRE peak versus ESF occurrence index (see text for explanation) for three different seasons and solar flux conditions. The red markers in December indicate significant ESF events that followed negative PRE peaks in 24 and 25 January 2008.

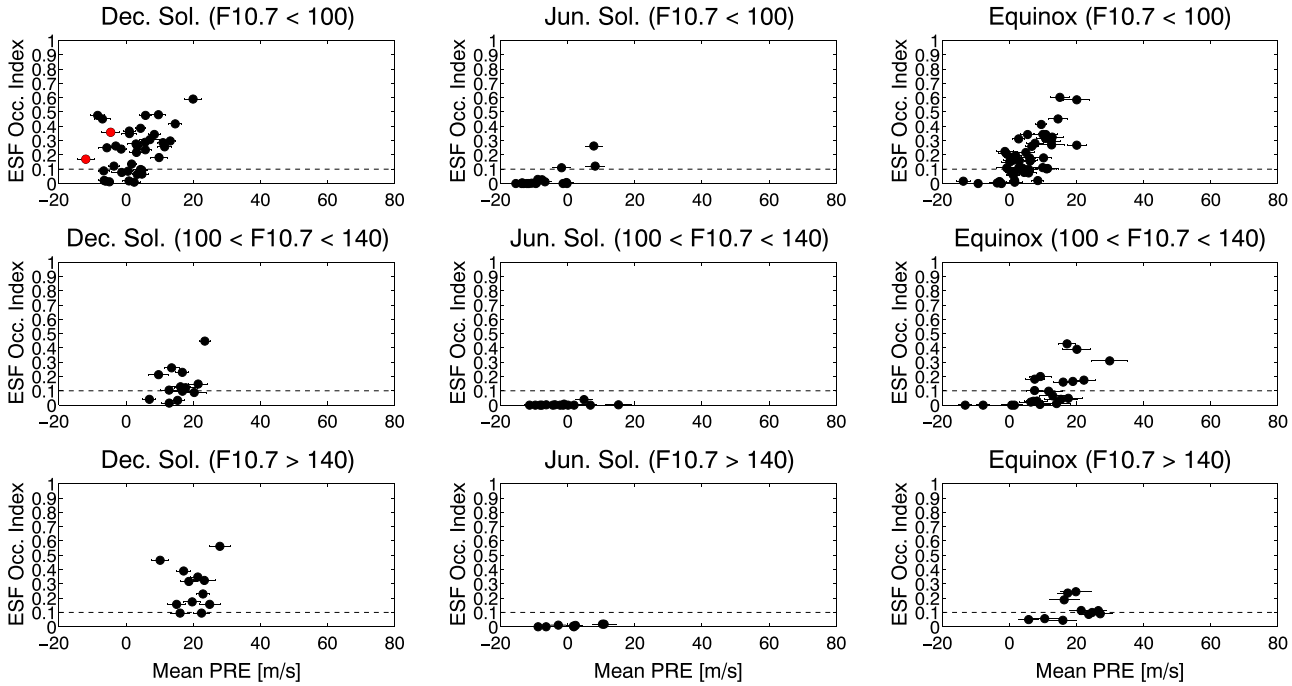

Figure 8. Mean PRE versus ESF occurrence index (see text for explanation) for three different seasons and solar flux conditions. The red markers in December indicate significant ESF events that followed negative PRE peaks in 24 and 25 January 2008.

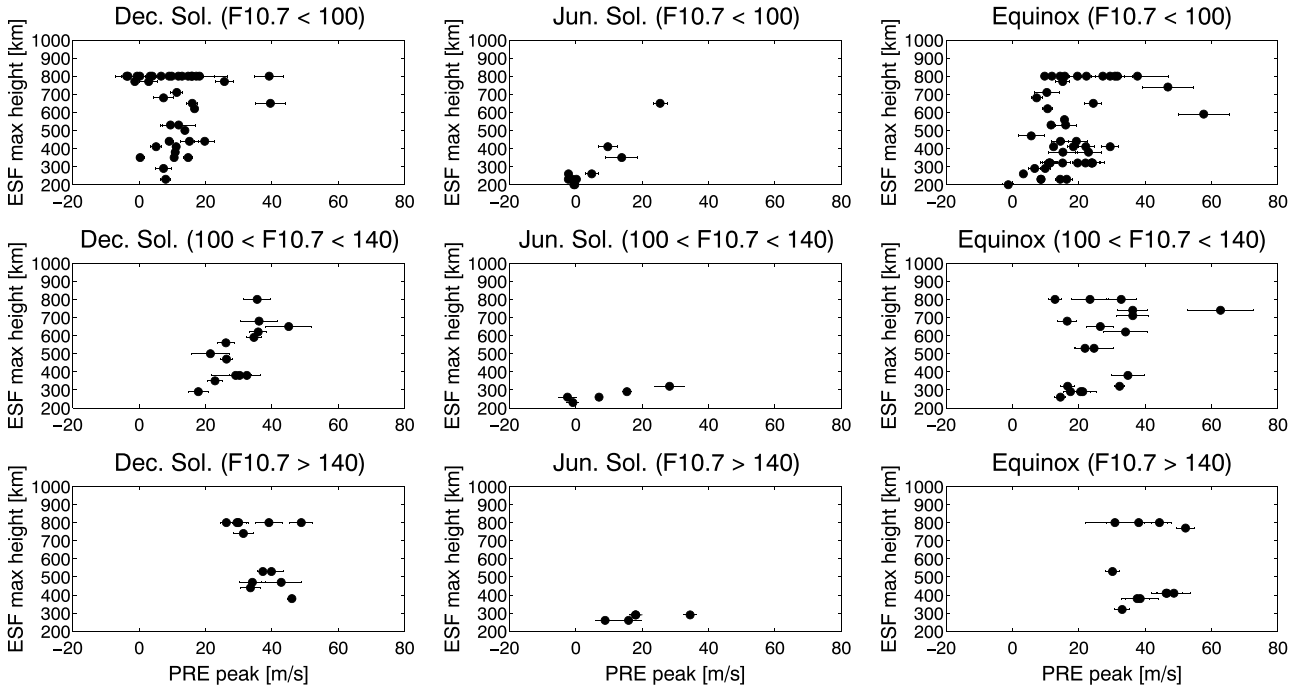

Figure 9. PRE peak versus maximum ESF height (see text for explanation) for three different seasons and solar flux conditions.

for instance, data points when the variability of the mean drifts exceeded 10 m/s. We also only considered days when at least 75% of the possible ESF observations between 1900 and 2400 LT were available. We removed cases when large gaps of data existed. These data gaps generally occur because observations were concluded or were temporarily stopped due to technical issues.

Figure 7 shows the ESF occurrence index as a function of the PRE peak. The error bars represent the variability (in height and time) of the drifts used to compute the PRE peak value. The dashed line indicates the 0.1 ESF

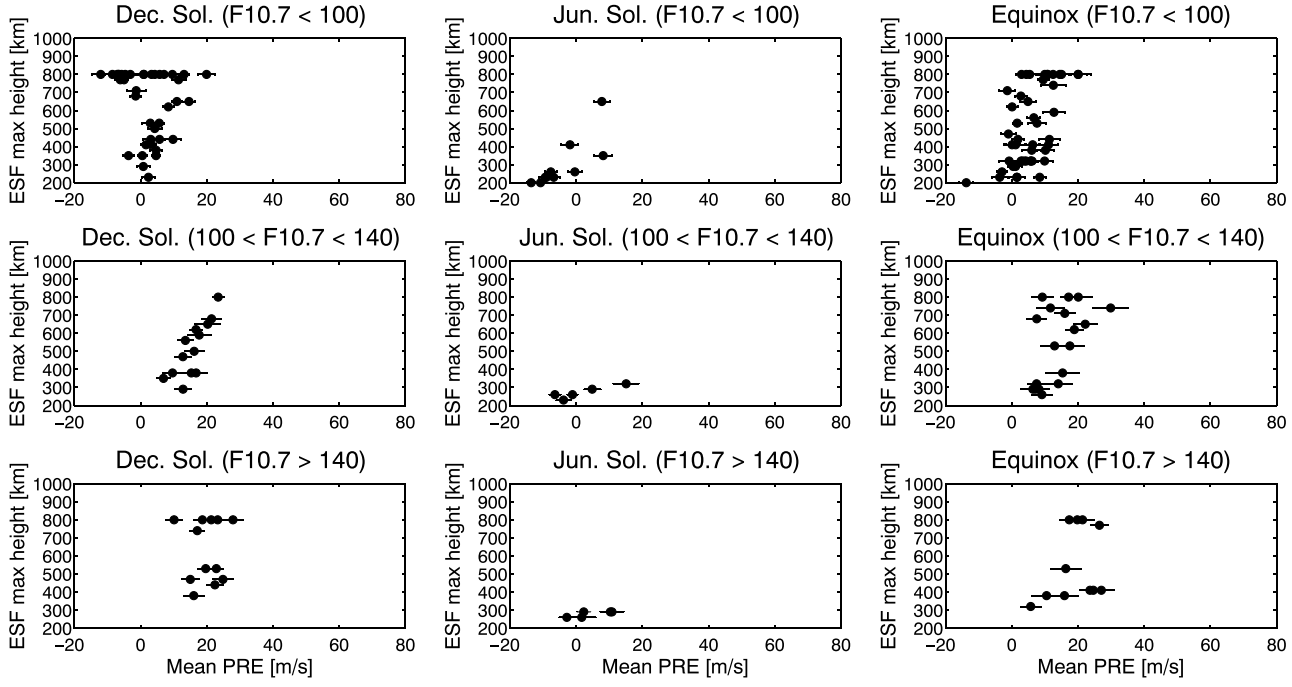

Figure 10. Mean PRE versus maximum ESF height (see text for explanation) for three different seasons and solar flux conditions.

occurrence index as a reference. In terms of the PRE peak values, the panels show that as solar flux increases, the likelihood of finding larger PRE peaks also increases. For instance, during December solstice LSF conditions, most of the PRE peaks are between 0 and 20 m/s. At HSF conditions, however, the PRE peak values range between 20 and 50 m/s. A similar trend is observed during equinox. The trend is not as clear during June solstice due to, at least in part, a reduced number of observations. During June, most PRE peak values are within −10 and 20 m/s. During MSF and HSF conditions, only a couple of cases of PRE peak values greater than 20 m/s were observed. Regarding ESF occurrence index, the results in Figure 7 show that this value ranges from 0 (no ESF) to 0.7 (70% occurrence between 200 and 800 km altitude and between 1900 and 2400 LT). For December solstice, PRE peak values causing significant ESF (occurrence index > 0.1) are typically greater than ∼−5 m/s during LSF, greater than ∼20 m/s for MSF, and greater than ∼25 m/s for HSF conditions. For equinox, the PRE peaks associated with significant ESF are typically greater than ∼+5 m/s during LSF, greater than ∼15 m/s during MSF, and greater than 30 m/s during HSF conditions. The results also illustrate a wide range of ESF occurrence index values occurring for similar values of PRE peak. For instance, for December solstice and LSF, a PRE peak of about 10 m/s can precede ESF severities ranging from ∼0 to ∼0.5.

December solstice LSF appears to be an interesting period as our results reveal that weak PRE peaks (even negative) preceded strong ESF events. Negative PRE peaks followed by ESF events are indicated by red markers in Figure 7. These results indicate that, in addition to PRE peak, other factors play a role in ESF development. This is not surprising, since the GRT can be affected by other geophysical parameters such as thermospheric winds, off-equatorial *E* region conductivities, and the history of the vertical drifts. To our knowledge, this is the first reporting of radar observations showing strong ESF events following a negligible PRE peak. We also found that these two exceptional cases occurred during SSW events. Using satellite measurements, *Huang and Hairston* [2015] also found a few unusual cases of small (or downward) PRE peaks producing weak plasma density perturbations (i.e., weak ESF).

In the past, it has been suggested that a threshold PRE peak produces the necessary conditions for ESF development, and that this threshold changes with solar flux [*Fejer et al.*, 1999]. As the PRE moves the *F* layer to higher altitudes, the ion-neutral collision frequency is reduced, contributing to an increased GRT growth rate and ESF development. The study by *Redmon et al.* [2010] found that the height of the bottomside *F* layer, which depends on the vertical plasma drift, must reach a threshold value for significant ESF (VHF scintillation) to be observed. They also found that the threshold height increases with solar flux. Our results tend to agree with these studies but we must emphasize that a PRE peak of certain magnitude is not a sufficient condition. Figure 7 shows several cases of large PRE peaks which were not associated with severe ESF events. Additionally, limitations in the existing set of measurements must be pointed out. During MSF and HSF conditions, only a few cases of weak (<20 m/s) PRE peak cases were observed. These cases occurred, mostly, during equinox MSF and support that a PRE greater than ∼15 m/s is necessary for ESF development. For PRE peak <15 m/s, ESF did not develop. A more definite conclusion requires additional drift and ESF measurements during MSF and HSF conditions as we only have a few cases of drifts and ESF during nights of weak (<15 m/s) PRE peak. Unfortunately, the number of hours of incoherent scatter radar measurements is severely limited to about 1000 h per year to be distributed among different experiments.

Based on our results in Figure 7, it can also be seen that a PRE of certain magnitude is not a sufficient condition for the occurrence of ESF. We can identify cases where strong PRE peaks (>20 m/s) were not associated with severe ESF, especially during MSF conditions in December solstice and equinox. *Huang and Hairston* [2015] also determined that significant PRE peaks (as large as 69 m/s) can occur without plasma bubbles (i.e., ESF). The role of other geophysical factors as well as the effects of other plasma instability processes in ESF development has recently started to be investigated using a data-driven modeling approach [e.g., *Hysell et al.*, 2014].

Figure 8 shows our results of ESF occurrence index as a function of the mean PRE. Similar to our analyses of the PRE peak, we found that the mean PRE increases with solar flux during December solstice and equinox conditions. During June, the solar flux control of the drifts is not as clear. Again, we also find that the results have a tendency of a threshold mean PRE for the occurrence of significant ESF (occurrence index > 0.1). For December solstice, the thresholds are ∼−10 m/s, ∼10 m/s, and ∼10 m/s for LSF, MSF, and HSF, respectively. For equinox conditions, the thresholds are ∼0 m/s, ∼10 m/s, and ∼18 m/s for LSF, MSF, and HSF, respectively. The thresholds of mean PRE are typically higher for equinox than for December solstice, similar to what we found in our PRE peak results. This might be caused by the quick reversal followed by large downward drifts that are

more commonly observed during equinox than December (see Figure 5). The quick reversal and downward drifts seem to contribute significantly to inhibiting ESF development during equinox.

Finally, Figures 9 and 10 show our results: the ESF maximum height ("ESFmax ht") versus PRE peak and mean PRE, respectively. We did not find a clear relationship between the PRE magnitude and the maximum height of ESF. This is, in part, due to the fact that ISR measurements are limited to a maximum altitude of about 800 km. Previous studies using coherent scatter radar measurements with higher ranges show that the maximum height of ESF increases with solar flux and possibly with the PRE magnitude [e.g., *Chapagain et al.*, 2009; *Cueva et al.*, 2013]. We found that ESF can reach 800 km altitude even during LSF conditions in December and equinox. During June, ESF is limited to bottom-type and bottomside layers occurring at heights below ~450 km, with only one exception in our data set.

4. Conclusions

We report the results of a comprehensive analysis of almost 20 years (1994–2013) of measurements made by the Jicamarca incoherent scatter radar (ISR). Our work expands previous studies of ESF and drifts at Jicamarca and provides new insights based on measurements and analyses that are now possible. For instance, the improved ISR measurements [*Kudeki et al.*, 1999] used here allowed us to estimate drifts at heights and local times that were not possible in the study of, e.g., *Fejer et al.* [1999]. Also, we used metrics of the evening drifts and ESF occurrence to better quantify the relationship between the pre-reversal enhancement (PRE) and irregularity development than previously possible.

ISR drift mode [*Kudeki et al.*, 1999] was used to investigate the quiet-time behavior of the equatorial *F* region plasma drifts and equatorial spread *F* (ESF) events during different solar flux and seasonal conditions. We constructed maps (local time versus height) of the occurrence of ESF irregularities and curves of mean *F* region drifts for each observation day. Then, we used the results of our daily analysis to derive the ESF occurrence rate and mean *F* region drifts as a function of season (June and December solstice, and equinox) and three ranges of solar flux conditions (low: $F_{10.7} < 100$, moderate: $100 \leq F_{10.7} \leq 140$, and high: $F_{10.7} > 140$ SFU). Finally, we also investigated the relationship between the pre-reversal enhancement (PRE) and the development of ESF events on a day-to-day basis. For that purpose, we proposed and evaluated two metrics of the PRE magnitude ("PRE peak" and "mean PRE") and two metrics of the ESF development ("ESF occurrence index" and "ESF maximum height").

The main findings of our investigation are summarized below:

1. The vertical drifts and ESF occurrence observed over the past two solar cycles (1994–2013) follow, in general, the pattern estimated from independent sets of measurements and techniques, and during other periods of time [e.g., *Hysell and Burcham*, 2002; *Scherliess and Fejer*, 1999]. To a first order, the behavior in ESF occurrence, for different solar flux and seasonal conditions, can be explained by the mean vertical plasma drifts.
2. We found, however, a higher than expected occurrence rate of post-midnight ESF during December solstice, low solar flux conditions. The maps of echo occurrence and analysis of individual observations indicate that the post-midnight irregularities are an extension of pre-midnight ESF. The measurements made during these conditions contained many campaign observations during SSW events. Despite the abnormal *F* region drift conditions observed in the afternoon/evening sector during SSW events, we found that ESF can be very strong, well developed in altitude, and last several hours past local midnight. However, the unusually high occurrence of ESF during December solstice at low solar flux conditions could also be due to the abnormally contracted ionosphere during the extreme solar minimum of 2008/2009.
3. The results revealed the production of severe ESF events despite weak PRE peaks. Surprisingly, we even found cases of negative PRE peaks producing significant ESF during December solstice, low solar flux conditions. During low solar flux conditions, the requirement of a large upward drift is not crucial as the ionosphere is more contracted. A small drift enhancement can raise the *F* layer to altitudes where the ion-neutral collision frequency is low enough to significantly affect the ESF growth rate.
4. Our results tend to agree with the hypothesis of a threshold PRE for conditions leading to ESF development [e.g., *Fejer et al.*, 1999]. The threshold value, as previously suggested, does vary with solar flux and also with season. Table 1 provides our initial estimates based on the data sets used in this study. Additional observational efforts, however, are necessary to properly test and better determine the proposed threshold values. In particular, more observations of drifts and *F* region irregularities during weak PRE events at moderate and

Table 1. Approximate Values of Observed Minimum PRE Peak and Mean PRE Values Preceding Significant ESF Events (ESF Occurrence Index > 0.1) for December Solstice and Equinox and for Three Different Solar Flux Conditions (Low (i.e., LSF): $F_{10.7}$ < 100 SFU, Moderate (i.e., MSF): 100 < $F_{10.7}$ < 140 SFU, High (i.e., HSF): $F_{10.7}$ > 140 SFU)[a]

	PRE Peak		Mean PRE	
	Dec Solstice	Equinox	Dec Solstice	Equinox
LSF	−5.0 [0.0] m/s	5.0 m/s	−10 [−5.0] m/s	0.0 m/s
MSF	20 m/s	15 m/s	10 m/s	10 m/s
HSF	25 m/s	30 m/s	10 m/s	18 m/s

[a]The values in square brackets for December solstice have been obtained by neglecting the abnormal results of 24 and 25 January 2008. We note that these thresholds are initial estimates, and more observations are needed to obtain more definitive results.

high solar flux conditions are needed. A combination of ESF measurements made by low-power coherent scatter radars and drift measurements made by satellite sensors might provide such observations. These values can serve as a guide for future studies and improvements of the threshold estimation. We must point out that our mean *F* region drifts were derived from 200 to 400 km altitude. The drifts, however, have been shown to vary with height, particularly during evening hours [*Fejer et al.*, 2014].

5. We found that despite large PRE peaks, ESF might not occur. A PRE peak (or mean evening drifts) of a certain value does not provide sufficient conditions for ESF development. This reinforces that other geophysical factors (conductivity, density gradients, neutrals winds, and instability processes) play a significant role in ESF development and variability.
6. ESF irregularities can reach altitudes at least as high as 800 km even during low solar flux conditions. During June solstice, ESF events rarely exceeded 500 km altitude. The ESF height estimate can be useful for upcoming satellite-based studies of ESF and associated phenomena.

Acknowledgments
The radar measurements used in this study can be obtained from the Madrigal database at http://jro.igp.gob.pe. The Jicamarca Radio Observatory is a facility of the Instituto Geofisico del Peru operated with support from the NSF AGS-1433968 through Cornell University. Work at UT Dallas was supported by NSF AGS-1261107 and AFOSR FA9550-13-1-0095.

References

Abdu, M. A. (2001), Outstanding problems in the equatorial ionosphere–thermosphere electrodynamics relevant to spread *F*, *J. Atmos. Sol. Terr. Phys.*, *63*(9), 869–884.

Abdu, M. A., E. Alam Kherani, I. S. Batista, E. R. de Paula, D. C. Fritts, and J. H. A. Sobral (2009), Gravity wave initiation of equatorial spread *F*/plasma bubble irregularities based on observational data from the SpreadFEx campaign, *Ann. Geophys.*, *27*, 2607–2622, doi:10.5194/angeo-27-2607-2009.

Anderson, D. N., B. Reinisch, C. Valladares, J. Chau, and O. Veliz (2004), Forecasting the occurrence of ionospheric scintillation activity in the equatorial ionosphere on a day-to-day basis, *J. Atmos. Sol. Terr. Phys.*, *66*(17), 1567–1572, doi:10.1016/j.jastp.2004.07.010.

Aveiro, H. C., and D. L. Hysell (2010), Three-dimensional numerical simulation of equatorial *F* region plasma irregularities with bottomside shear flow, *J. Geophys. Res.*, *115*, A11321, doi:10.1029/2010JA015602.

Basu, S., S. Basu, J. Aarons, J. P. McClure, and M. D. Cousins (1978), On the coexistence of kilometer- and meter-scale irregularities in the nighttime equatorial *F* region, *J. Geophys. Res.*, *83*(A9), 4219–4226, doi:10.1029/JA083iA09p04219.

Basu, S., et al. (1996), Scintillations, plasma drifts, and neutral winds in the equatorial ionosphere after sunset, *J. Geophys. Res.*, *101*(A12), 26,795–26,809, doi:10.1029/96JA00760.

Basu, B. (2002), On the linear theory of equatorial plasma instability: Comparison of different descriptions, *J. Geophys. Res.*, *107*(A8), 1199, doi:10.1029/2001JA000317.

Booker, H. G., and H. W. Wells (1938), Scattering of radio waves in the *F*-region of ionosphere, *Terr. Mag. Atmos. Elec.*, *43*, 249–256.

Candido, C. M. N., I. S. Batista, F. Becker-Guedes, M. A. Abdu, J. H. A. Sobral, and H. Takahashi (2011), Spread *F* occurrence over a southern anomaly crest location in Brazil during June solstice of solar minimum activity, *J. Geophys. Res.*, *116*, A06316, doi:10.1029/2010JA016374.

Chapagain, N. P., B. G. Fejer, and J. L. Chau (2009), Climatology of postsunset equatorial spread *F* over Jicamarca, *J. Geophys. Res.*, *114*, A07307, doi:10.1029/2008JA013911.

Chau, J. L., B. G. Fejer, and L. P. Goncharenko (2009), Quiet variability of equatorial E × B drifts during a sudden stratospheric warming event, *Geophys. Res. Lett.*, *36*, L05101, doi:10.1029/2008GL036785.

Cueva, R. Y. C., E. R. de Paula, and A. E. Kherani (2013), Statistical analysis of radar observed *F* region irregularities from three longitudinal sectors, *Ann. Geophys.*, *31*, 2137–2146, doi:10.5194/angeo-31-2137-2013.

de La Beaujardiere, O. et al. (2009), C/NOFS observations of deep plasma depletions at dawn, *Geophys. Res. Lett.*, *36*, L00C06, doi:10.1029/2009GL038884.

Fejer, B. G., L. Scherliess, and E. R. de Paula (1999), Effects of the vertical plasma drift velocity on the generation and evolution of equatorial spread *F*, *J. Geophys. Res.*, *104*(A9), 19,859–19,869, doi:10.1029/1999JA900271.

Fejer, B. G., J. W. Jensen, and S.-Y. Su (2008), Quiet time equatorial *F* region vertical plasma drift model derived from ROCSAT-1 observations, *J. Geophys. Res.*, *113*, A05304, doi:10.1029/2007JA012801.

Fejer, B. G., D. Hui, J. L. Chau, and E. Kudeki (2014), Altitudinal dependence of evening equatorial *F* region vertical plasma drifts, *J. Geophys. Res. Space Physics*, *119*, 5877–5890, doi:10.1002/2014JA019949.

Fesen, C. G., G. Crowley, R. G. Roble, A. D. Richmond, and B. G. Fejer (2000), Simulation of the pre-reversal enhancement in the low latitude vertical ion drifts, *Geophys. Res. Lett.*, *27*(13), 1851–1854, doi:10.1029/2000GL000061.

Heelis, R. A., P. C. Kendall, R. J. Moffet, D. W. Windle, and H. Rishbeth (1974), Electrical coupling of the *E* and *F* regions and its effect on the *F* region drifts and winds, *Planet. Space Sci.*, *22*, 743–756, doi:10.1016/0032-0633(74)90144-5.

Heelis, R. A., W. R. Coley, A. G. Burrell, M. R. Hairston, G. D. Earle, M. D. Perdue, R. A. Power, L. L. Harmon, B. J. Holt, and C. R. Lippincott (2009), Behavior of the O+/H+ transition height during the extreme solar minimum of 2008, *Geophys. Res. Lett.*, *36*, L00C03, doi:10.1029/2009GL038652.

Huang, C.-S., and M. C. Kelley (1996), Nonlinear evolution of equatorial spread *F*: 2. Gravity wave seeding of Rayleigh-Taylor instability, *J. Geophys. Res.*, *101*(A1), 293–302, doi:10.1029/95JA02210.

Huang, C.-S., and M. R. Hairston (2015), The postsunset vertical plasma drift and its effects on the generation of equatorial plasma bubbles observed by the C/NOFS satellite, *J. Geophys. Res. Space Physics*, *120*, 2263–2275, doi:10.1002/2014JA020735.

Huang, C.-S., O. de La Beaujardiere, R. F. Pfaff, J. M. Retterer, P. A. Roddy, D. E. Hunton, Y.-J. Su, S.-Y. Su, and F. J. Rich (2010), Zonal drift of plasma particles inside equatorial plasma bubbles and its relation to the zonal drift of the bubble structure, *J. Geophys. Res.*, *115*, A07316, doi:10.1029/2010JA015324.

Huang, C.-S., O. de La Beaujardiere, P A. Roddy, D. E. Hunton, J. O. Ballenthin, and M. R. Hairston (2012), Generation and characteristics of equatorial plasma bubbles detected by the C/NOFS satellite near the sunset terminator, *J. Geophys. Res.*, *117*, A11313, doi:10.1029/2012JA018163.

Hysell, D. L. (2000), An overview and synthesis of plasma irregularities in equatorial spread-*F*, *J. Atmos. Sol.-Terr. Phys.*, *62*(12), 1037–1056.

Hysell, D. L., and J. D. Burcham (1998), JULIA radar studies of equatorial spread *F*, *J. Geophys. Res.*, *103*(A12), 29,155–29,167, doi:10.1029/98JA02655.

Hysell, D. L., and J. D. Burcham (2002), Long term studies of equatorial spread F using the JULIA radar at Jicamarca, *J. Atmos. Sol.-Terr. Phys.*, *64*(12–14), 1531–1543.

Hysell, D. L., and E. Kudeki (2004), Collisional shear instability in the equatorial *F* region ionosphere, *J. Geophys. Res.*, *109*, A11301, doi:10.1029/2004JA010636.

Hysell, D. L., J. Chun, and J. L. Chau (2004), Bottom-type scattering layers and equatorial spread *F*, *Ann. Geophys.*, *22*, 4061–4069, doi:10.5194/angeo-22-4061-2004.

Hysell, D. L., R. Jafari, M. A. Milla, and J. W. Meriwether (2014), Data-driven numerical simulations of equatorial spread *F* in the Peruvian sector, *J. Geophys. Res. Space Physics*, *119*, 3815–3827, doi:10.1002/2014JA019889.

Jayachandran, B., N. Balan, P. B. Rao, J. H. Sastri, and G. J. Bailey (1993), HF Doppler and ionosonde observations on the onset conditions of equatorial spread *F*, *J. Geophys. Res.*, *98*(A8), 13,741–13,750, doi:10.1029/93JA00302.

Kelley, M. C. (1989), *The Earth's Ionosphere: Plasma Physics and Electrodynamics*, Academic Press, San Diego, Calif.

Kelley, M. C., M. F. Larsen, C. LaHoz, and J. P. McClure (1981), Gravity wave initiation of equatorial spread *F*: A case study, *J. Geophys. Res.*, *86*(A11), 9087–9100, doi:10.1029/JA086iA11p09087.

Kelley, M. C., R. C. Livingston, C. L. Rino, and R. T. Tsunoda (1982), The vertical wave number spectrum of topside equatorial spread *F*: Estimates of backscatter levels and implications for a unified theory, *J. Geophys. Res.*, *87*(A7), 5217–5221, doi:10.1029/JA087iA07p05217.

Kil, H., and R. A. Heelis (1998), Global distribution of density irregularities in the equatorial ionosphere, *J. Geophys. Res.*, *103*(A1), 407–417, doi:10.1029/97JA02698.

Kil, H., S.-J. Oh, L. J. Paxton, and T.-W. Fang (2009), High-resolution vertical E B drift model derived from ROCSAT-1 data, *J. Geophys. Res.*, *114*, A10314, doi:10.1029/2009JA014324s.

Krall, J., J. D. Huba, G. Joyce, and S. T. Zalesak (2009), Three-dimensional simulation of equatorial spread-*F* with meridional wind effects, *Ann. Geophys.*, *27*, 1821–1830, doi:10.5194/angeo-27-1821-2009.

Kudeki, E., S. Bhattacharyya, and R. F. Woodman (1999), A new approach in incoherent scatter F region E B drift measurements at Jicamarca, *J. Geophys. Res.*, *104*(A12), 28,145–28,162, doi:10.1029/1998JA900110.

Kudeki, E., A. Akgiray, M. A. Milla, J. L. Chau, and D. L. Hysell (2007), Equatorial spread-F initiation: Post-sunset vortex, thermospheric winds, gravity waves, *J. Atmos. Sol. Terr. Phys.*, *69*(17–18), 2416–2427.

Maruyama, T., and N. Matuura (1984), Longitudinal variability of annual changes in activity of equatorial spread *F* and plasma bubbles, *J. Geophys. Res.*, *89*, 10,903–10,912.

Mendillo, M., J. Meriwether, and M. Biondi (2001), Testing the thermospheric neutral wind suppression mechanism for day-to-day variability of equatorial spread *F*, *J. Geophys. Res.*, *106*(A3), 3655–3663, doi:10.1029/2000JA000148.

Redmon, R. J., D. Anderson, R. Caton, and T. Bullett (2010), A Forecasting Ionospheric Real-time Scintillation Tool (FIRST), *Space Weather*, *8*, S12003, doi:10.1029/2010SW000582.

Retterer, J. M., and L. C. Gentile (2009), Modeling the climatology of equatorial plasma bubbles observed by DMSP, *Radio Sci.*, *44*, RS0A31, doi:10.1029/2008RS004057.

Rodrigues, F. S., A. O. Moraes, and E. R. dePaula (2012a), Imaging equatorial spread *F* irregularities with the São Luís coherent backscatter radar interferometer, *Radio Sci.*, *47*, RS0L03, doi:10.1029/2011RS004929.

Rodrigues, F. S., G. Crowley, R. A. Heelis, A. Maute, and A. Reynolds (2012b), On TIE-GCM simulation of the evening equatorial plasma vortex, *J. Geophys. Res.*, *117*, A05307, doi:10.1029/2011JA017369.

Scherliess, L., and B. G. Fejer (1999), Radar and satellite global equatorial *F* region vertical drift model, *J. Geophys. Res.*, *104*(A4), 6829–6842.

Stolle, C., H. Lhr, and B. G Fejer (2008), Relation between the occurrence rate of ESF and the equatorial vertical plasma drift velocity at sunset derived from global observations, *Ann. Geophys.*, *26*, 3979–3988, doi:10.5194/angeo-26-3979-2008.

Su, S.-Y., C. K. Chao, and C. H. Liu (2008), On monthly/seasonal/longitudinal variations of equatorial irregularity occurrences and their relationship with the postsunset vertical drift velocities, *J. Geophys. Res.*, *113*, A05307, doi:10.1029/2007JA012809.

Sultan, P. J. (1996), Linear theory and modeling of the Rayleigh-Taylor instability leading to the occurrence of equatorial spread *F*, *J. Geophys. Res.*, *101*(A12), 26,875–26,891, doi:10.1029/96JA00682.

Sulzer, M. P., and S. Gonzalez (1999), The effect of electron Coulomb collisions on the incoherent scatter spectrum in the *F* region at Jicamarca, *J. Geophys. Res.*, *104*(A10), 22,535–22,551, doi:10.1029/1999JA900288.

Tsunoda, R. T. (2010), On seeding equatorial spread *F* during solstices, *Geophys. Res. Lett.*, *37*, L05102, doi:10.1029/2010GL042576.

Tsunoda, R. T., R. C. Livingston, and C. L. Rino (1981), Evidence of a velocity shear in bulk plasma motion associated with the post-sunset rise of the equatorial *F*-layer, *Geophys. Res. Lett.*, *8*(7), 807–810.

Watanabe, S., and H. Oya (1986), Occurrence characteristics of low latitude ionospheric irregularities observed by the impedance probe on board the Hinotori satellite, *J. Geomagn. Geoelectr.*, *38*, 135–149, doi:10.5636/jgg.38.125.

Woodman, R. F. (2009), Spread *F* an old equatorial aeronomy problem finally resolved, *Ann. Geophys.*, *27*, 1915–1934, doi:10.5194/angeo-27-1915-2009.

Woodman, R. F., and T. Hagfors (1969), Methods for the measurement of vertical ionospheric motions near the magnetic equator by incoherent scattering, *J. Geophys. Res.*, *74*(5), 1205–1212, doi:10.1029/JA074i005p01205.

Woodman, R. F., and C. La Hoz (1976), Radar observations of *F* region equatorial irregularities, *J. Geophys. Res.*, *81*, 5447–5466.

Zhang, S.-R., S. Fukao, W. L. Oliver, and Y. Otsuka (1999), The height of the maximum ionospheric electron density over the MU radar, *J. Atmos. Sol. Terr. Phys.*, *61*, 1367–1383, doi:10.1016/S1364-6826(99)00088-7.